



1 Quantitative effects of antecedent effective rainfall on *ID* threshold for debris flow

2 Shaojie Zhang <sup>1</sup>, Hongjuan Yang <sup>1</sup>, Dunlong Liu <sup>2</sup>, Kaiheng Hu<sup>1</sup>, Fangqiang Wei<sup>1</sup>

3 1. Key Laboratory of Mountain Hazards and Earth Surface Process, Institute of Mountain Hazards and  
4 Environment, Chinese Academy of Sciences, Chengdu 610041, China

5 2.College of Software Engineering, Chengdu University of Information and Technology, Chengdu, 610225, China

6 Correspondence to: K.H. Hu, E-mail: [khhu@imde.ac.cn](mailto:khhu@imde.ac.cn), F.Q. Wei, E-mail: [fqwei@imde.ac.cn](mailto:fqwei@imde.ac.cn)

7

## 8 **Abstract**

9 Studies have shown that the antecedent effect precipitation (*AEP*) is closely related to rainfall  
10 intensity-duration (*ID*) threshold of debris flow. However, the quantitative relationship between  
11 the *AEP* and *ID* threshold is still undetermined. In this study, a hydrological process based  
12 numerical model (*Dens-ID*) that can derive the *ID* threshold curve is adopted to address this issue.  
13 Jiangjia Gully (*JJG*) in Dongchuan District of Yunnan Province was chosen as the study area,  
14 *Dens-ID* was used to derive a series of *ID* threshold curves corresponding to different *AEP*. Based  
15 on calculated data sets including *AEP*, *ID* curves, parameters of *ID* curve equation ( $\alpha$  and  $\beta$ ), and  
16 debris flow density, the influence of *AEP* on the *ID* threshold curve is deeply explored. We found  
17 that although solid materials and runoff are the two necessary conditions for the formation of  
18 debris flow, the specific roles played in which are different: the volume of loose solid sources  
19 provides a basal condition for debris flow and determines the scale of debris flow, while the runoff  
20 volume will have a sudden change during the rainfall process, which is a key factor promoting the  
21 formation of debris flow. In the condition of *AEP* ranging from 20 mm to 90 mm, *AEP* and  $\alpha$  can



22 be described by the equation  $\alpha = -0.0078AEP^2 + 0.68AEP + 6.43$ , and  $\beta$  shows a linear change law  
23 with  $AEP$ . The error of the two equations were evaluated using 45 historical rainfall data that  
24 triggered debris flows, which is equal to 37.85% and 11.1%. Due to the two functions, the ID  
25 threshold curve can regularly move in the I-D coordinate system rather than a conventional  
26 threshold curve stay the same regardless of  $AEP$  variation, it is beneficial to improve the  
27 prediction capacity of the ID threshold.

## 28 **1 Introduction**

29 Precipitation that affects debris flow formation includes triggering rainfall and antecedent  
30 effective precipitation (AEP) before the event (Chen et al., 2015; Chen et al., 2018; Oorthuis et al.,  
31 2021). AEP is precipitation that remains in soil before a debris flow occurs; it reflects the degree  
32 of soil saturation (Zhang et al., 2015). Increased AEP, and thus increased moisture content, has  
33 been shown to enhance surface rainfall-induced runoff in various environments (Tisdall, 1951;  
34 Luk, 1985; Le Bissonnais et al., 1995; Castillo et al., 2003; Jones et al., 2017). Additionally, the  
35 increased soil water content caused by AEP decreases the shear strength of the loose soil mass in a  
36 debris flow gully, enhancing the supply rate of the solid material required for debris flow  
37 formation (Lehmann and Or, 2012; Kim et al., 2013; Ruetter et al., 2014). AEP has an important  
38 effect on the rainfall threshold for triggering debris flow. Debris flow prediction can be improved  
39 by quantifying this effect (Chen et al., 2018; Zhao et al., 2019; Hirschberg et al., 2021; Marino et  
40 al., 2020; Jiang et al., 2021).

41 A rainfall threshold is generally a fixed value of some rainfall parameter such as cumulative  
42 rainfall, hourly rainfall intensity, or AEP (Marra et al., 2017); alternatively, it can be a curve of  
43 two rainfall parameters (Peres and Cancelliere, 2014), such as the rainfall intensity–rainfall



44 duration threshold curve (Cain, 1980) and rainfall intensity–antecedent rainfall curve (Long et al.,  
45 2020). The most commonly investigated threshold is the intensity ( $I$ ) versus duration ( $D$ ) curve  
46 (Crosta and Frattini, 2003; Cannon et al., 2008; Guzzetti et al., 2008; Berti et al., 2020), which has  
47 the form  $I = \alpha D^\beta$ , where  $I$  represents the average rain intensity in the rainfall process that triggers  
48 debris flow,  $D$  represents the rainfall duration, and  $\alpha$  and  $\beta$  are empirical parameters. Segoni et al.  
49 (2018) analyzed the rainfall thresholds of landslides and debris flows reported in 107 articles and  
50 found that the threshold model based on the  $ID$  threshold curve accounted for the highest  
51 proportion, approximately 48.6%. Empirical and process-based methods are commonly used to  
52 derive the  $ID$  threshold curves of debris flow (Segoni et al., 2018). The empirical model workflow  
53 is as follows. Data on debris flow events and the associated rainfall in a target area are collected,  
54 and the  $I$  and  $D$  values of each rainfall process that triggered a debris flow event are calculated.  $D$   
55 and  $I$  are plotted on the  $x$  and  $y$  axes, respectively, and the  $ID$  threshold curve is fitted using these  
56 data. As for the process-based methods, a typical physical parameter ( $P_i$ ) that can represent debris  
57 flow occurrence in a gully is first chosen, and the change in this parameter has a certain threshold  
58 interval (e.g.,  $[P_{\text{low}}, P_{\text{upper}}]$ ). During a rainfall process,  $P_i$  changes because of hydrological  
59 processes such as rainfall infiltration and runoff. When it falls into the interval  $[P_{\text{low}}, P_{\text{upper}}]$ , a  
60 debris flow may be triggered under these rainfall conditions. Then a numerical model is built to  
61 calculate  $P_i$  by inputting different rainfall conditions characterized by different  $D$  and  $I$ . For a  
62 certain value of  $P_i$  (e.g.,  $P_{\text{upper}}$ ), the  $[D_i, I_i]$  data for which the calculated value is equal to  $P_{\text{upper}}$  are  
63 collected during model calculations. These collected data are then used to fit the threshold curves  
64 (Long et al., 2020). Papa et al. (2013) proposed that the total area ( $S$ ) of shallow landslides  
65 induced by rainfall in a gully plays an important role in debris flow formation. Therefore, the ratio



66 of  $S$  to the catchment area is used as the threshold (that is,  $P_i$ ), and the TRIGERS model (Baum et  
67 al., 2002, 2008) and a rainfall scenario simulation are adopted to calculate  $P_i$  and search for the  
68 combination of all  $[I_i, D_i]$  at which the  $P_i$  calculated by the model is equal to a preset value. Next,  
69 the  $ID$  threshold curve corresponding to this value is obtained by fitting. Although shallow  
70 landslides induced by rainfall in a basin are very important for debris flow formation, the effect of  
71 hydrodynamic conditions provided by rainfall-induced runoff on debris flow formation cannot be  
72 ignored. Scholars have argued that a water-soil mixture in a gully can be formed by coupling  
73 between the rainfall-induced solid material and runoff (Church and Jakob, 2020). The debris flow  
74 density represents the fluid characteristics of the mixture and can be used to incorporate the two  
75 major factors (rainfall-induced loose solid material and rainfall-induced runoff) that affect debris  
76 flow formation into numerical simulation models (Zhang et al., 2020; Long et al., 2020). A  
77 numerical model (Dens-ID) is used to correlate rainfall parameters with the density boundaries of  
78 1.2 and 2.2 g/cm<sup>3</sup>; the  $ID$  threshold curve of debris flow can then be constructed in the physical  
79 framework. The  $ID$  curve fitted by this model reportedly has a shape similar to that of the  
80 statistics-based curve. The precision of debris flow prediction by this model in Jiangjia Gully (JJG)  
81 in Yunnan Province, China, is approximately 80.5%, which is 27.7% higher than that of the  
82 statistics-based  $ID$  curve (Zhang et al., 2020).

83 It is difficult to introduce AEP as a dependent variable into the power function  $I = \alpha D^\beta$ .  
84 Attempts to analyze the effect of AEP on the parameters  $\alpha$  and  $\beta$  have resulted in the following  
85 consensus. A larger AEP can decrease the rainfall conditions triggering debris flow; however, an  
86 equation that describes the quantitative evolution of each parameter ( $\alpha$  or  $\beta$ ) with AEP has not  
87 been derived. Some studies have used the relationship between daily rainfall and antecedent



88 rainfall (Kim et al., 1991; Glade et al., 2000; Dahal and Hasegawa, 2008; Giannecchini et al.,  
89 2012) or a combination of daily rainfall intensity and rainfall duration (Hasnawir and Kubota,  
90 2008; Khan et al., 2012; Zhao et al., 2019; Kim et al., 2020; Yang et al., 2020) to investigate the  
91 effects of AEP on the rainfall threshold. Jiang et al. (2021) investigated the probabilistic rainfall  
92 thresholds for debris flows after the Wenchuan earthquake and found that antecedent precipitation  
93 plays an important role in long-duration rainfall-induced debris flows. Zhao et al. (2019)  
94 introduced the simulated antecedent soil moisture into a probabilistic threshold and found that it  
95 exhibited better prediction performance than the daily rainfall intensity and rainfall duration (*ED*)  
96 threshold. However, all of these studies lack a quantitative description of the effect of AEP on the  
97 rainfall threshold. This lack is attributed mainly to the absence of sufficient historical data  
98 including AEP, rainfall intensity, rainfall duration, and debris flow events, which makes it difficult  
99 to conduct differential analysis and to derive a function that quantitatively describes their  
100 relationship.

101 To quantify the effect of AEP on the *ID* threshold curve, JYG in Yunnan Province, China, was  
102 chosen as the study area, and the Dens-ID numerical model was used to build its *ID* threshold  
103 curve database. The mechanism by which AEP affects the *ID* threshold curve is thoroughly  
104 discussed using this database, and equations for the functions describing the relationships between  
105 AEP and the parameters  $\alpha$  and  $\beta$  were derived through data analysis.

## 106 2 Methods

### 107 2.1 Dens-ID

108 Shallow landslides and bed erosion are the two main sources of debris flow material; both



109 may be present in the same gully, but one type is always dominant (Gabet and Mudd, 2006; Berti  
110 and Simoni, 2005; Coe et al., 2008; Long et al., 2020). Debris flow gullies with shallow landslides  
111 as the source of solid materials are widely distributed in southwestern China (Zhang et al., 2020).  
112 **Dens-ID** focuses on landslide-dominated supply and is designed to derive the *ID* threshold curves  
113 of debris flow by calculating the debris flow density in rainfall scenario simulations. The key  
114 function of this model is to correlate debris flow density with rainfall parameters, as described by  
115 Zhang et al. (2020) and Long et al. (2020). Debris flows are complex mixtures of water,  
116 fragmented rock, and sediments of all sizes (Chmiel et al., 2020). Dens-ID simplifies this complex  
117 nonuniform flow (Iverson, 1997) as a water-soil mixture. The runoff amount [ $V_w(t)$ ] and amount  
118 of solid material [ $V_s(t)$ ] are taken as the two parameters contributing to debris flow formation.  
119 Using these two parameters as the inputs of Eq. 1, Dens-ID can calculate the density of the water-  
120 soil mixture.

$$121 \quad \rho_{mix}(t) = \frac{\rho_w V_w(t) + \rho_s V_s(t)}{V_{mix}(t)} \quad (1)$$

122 where  $\rho_{mix}(t)$  is the density of the water-soil mixture,  $\rho_w$  is the water density,  $\rho_s$  is the density of  
123 soil particles, and  $V_{mix}(t)$  is the volume of the water-soil mixture, which is the sum of  $V_w(t)$  and  
124  $V_s(t)$ .  $V_w(t)$  and  $V_s(t)$  are the key variables for correlating the debris flow density with the rainfall  
125 parameters, which can be derived by pixel-based hydrological simulation (Long et al., 2020).

126 Based on a digital elevation model (DEM) of a debris flow gully, Dens-ID uses the theory of  
127 runoff generation from excess precipitation to control the infiltration boundary in the topsoil  
128 (Zhang et al., 2014a). It then simulates the vertical water movement within the soil mass using the  
129 differential equation of Richards (1931).



130 Governing equation of infiltration border:  $-D(\theta) \frac{\partial \theta}{\partial z} + K(\theta) = I(t)$  (2)

131 Richards' differential equation:  $\frac{\partial \theta}{\partial t} = \frac{\partial}{\partial z} [D(\theta) \frac{\partial \theta}{\partial z}] - \frac{\partial K(\theta)}{\partial \theta}$  (3)

132 where  $\theta$  is the soil water content;  $D(\theta) = K(\theta)/(d\theta/d\psi)$  is the soil water diffusivity;  $z$  is the soil  
133 depth, which is positive downward along the soil depth, taking the topsoil as the origin;  $K(\theta)$  is  
134 the hydraulic conductivity;  $I(t)$  is the rainfall intensity; and  $\psi$  is the soil matric suction.

135 After the hydrological simulation, Dens-ID outputs the water soil content  $\theta(i, t)$ , soil matric  
136 suction  $\psi(i, t)$ , and runoff depth  $dw(i, t)$  for each pixel of the DEM. Dens-ID then calculates  $V_w(t)$   
137 using the runoff depth  $dw(i, t)$ , as shown in Eq. 4.

138 
$$V_w(t) = \sum_{i=1}^T \sum_{g=1}^n S_g * dw(i, t)$$
 (4)

139 where  $n$  represents the total number of grid cells that can generate runoff at time  $t$ , and  $V_w(t)$   
140 represents the total volume of runoff in a gully at time  $t$ . Using  $\theta(i, t)$  and  $\psi(i, t)$  as inputs, Dens-ID  
141 adopts an infinite slope model (Zhang et al., 2014b; Liu et al., 2016; Zhang et al., 2018) to  
142 calculate the unstable depth of each grid cell  $ds(j, t)$ . It then calculates  $V_s(t)$  using  $ds(j, t)$ , as shown  
143 in Eq. 5.

144 
$$V_s(t) = \sum_{i=1}^T \sum_{j=1}^m S_g * ds(j, t)$$
 (5)

145 where  $m$  represents the number of grid cells that can provide solid material at time  $t$ , and  $V_s(t)$  is  
146 the total volume of solid material in the gully at time  $t$ .

147 The mixture density can be derived by substituting various rainfall parameters, including  
148 rainfall intensity ( $I$ ) and rainfall duration ( $D$ ), into the right side of Eq. 2. Then Dens-ID can  
149 correlate the rainfall parameters with the debris flow density.

## 150 2.2 Derivation of $ID$ threshold curve using Dens-ID



151       The debris flow density varies between 1.2 and 2.3 g/cm<sup>3</sup>. The values within the interval [1.2,  
152 2.3] represent a density set. In nature, a debris flow with a density  $\rho_{\text{mix}}$  **cann** be triggered by high-  
153 intensity or long-duration rainfall. Inputting rainfall scenarios with different combinations of [ $I_i$ ,  
154  $D_i$ ] into Dens-ID makes it possible to simulate debris flow initiation by rainfall in nature. Using a  
155 given density value ( $\rho_{\text{mix}}$ ) during the calculation, Dens-ID collects all the [ $I_i$ ,  $D_i$ ] data that meet the  
156 conditions of the rainfall scenarios (Fig. 1). That is, when the selected [ $I_i$ ,  $D_i$ ] are used as input,  
157 the output of the model is equal to  $\rho_{\text{mix}}$ . The collected [ $I_i$ ,  $D_i$ ] values represent another data group,  
158 which is referred to as a rainfall parameter set. Each data point [ $I_i$ ,  $D_i$ ] corresponds to a unique  
159 value of  $\rho_{\text{mix}}$  within the density set; thus, the correlation between the rainfall parameters and debris  
160 flow density can then be established by Dens-ID. An  $ID$  curve can then be fitted through the  
161 collected [ $I_i$ ,  $D_i$ ] data to show the relationship between  $I$  and  $D$ . Each fitted  $ID$  curve corresponds  
162 to a unique  $\rho_{\text{mix}}$  within the density set, which is also considered to be the isodensity line (Zhang et  
163 al., 2020). Two values close to the left and right boundaries are chosen from the density set as  $\rho_{\text{mix}}$ ,  
164 and the  $ID$  threshold curve corresponding to these two density values can represent the lower and  
165 upper boundaries for debris flow formation. The  $ID$  curves corresponding to a density value  $\rho_{\text{mix}}$   
166 are fitted as follows:

167       Step 1: Assign values of 1.2 and 2.2 g/cm<sup>3</sup> to  $\rho_{\text{mix}}$ .

168       Step 2: Assign **a value to the AEP**. In nature, the AEP represents the antecedent soil moisture  
169 before the rainfall process that may trigger a debris flow. In Dens-ID, the natural debris flow gully  
170 is divided into a series of grid cells, and the AEP represents the soil moisture content of each grid  
171 cell before rainfall infiltration. Using the initial hydrological conditions represented by the AEP,  
172 Dens-ID simulates hydrological processes such as runoff and infiltration during the triggering





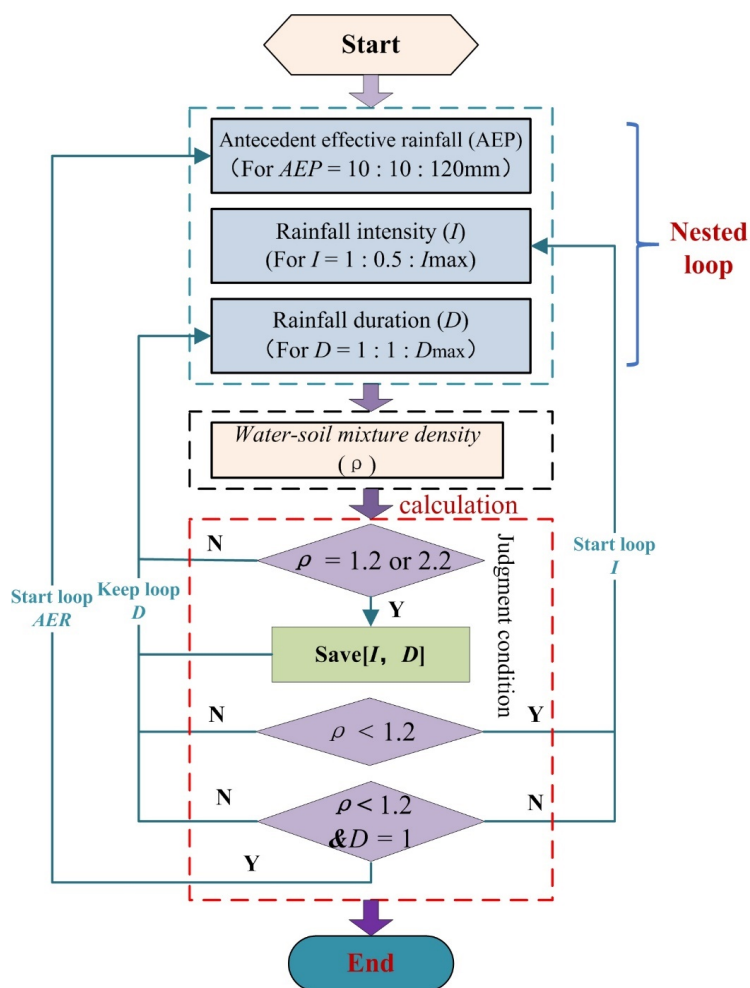
173 precipitation process. To quantitatively analyze the effect of AEP on the  $ID$  threshold curve, AEP<sub>*i*</sub>  
174 was assigned values of 10, 20, 30, 40, 50, 60, 70, 80, 90, 100, 110, and 120 mm.

175 Step 3: Assign a value to  $I_i$ , which generally represents the average rainfall intensity of a  
176 rainfall process that can trigger a debris flow and is held constant until the calculations in Step 4  
177 are complete. The initial value of  $I_i$  is set to 1 mm/h. When Step 4 is complete,  $I_i$  is increased by  
178 0.5 up to  $I_{\max}$ . At  $I_{\max}$ , a debris flow with density  $\rho_{\text{mix}}$  can be triggered in the gully when  $D = 1$ .

179 Step 4: Under constant  $I_i$ , the calculation time of the model starts at  $t = 1$  h and increases by 1  
180 h at each calculation step until  $t = D_i$ , where  $D_i$  represents the rainfall duration required to trigger a  
181 debris flow with density  $\rho_{\text{mix}}$ . After  $t = D_i$ , the model calculation for a given  $I_i$  is complete.

182 Step 5: Repeat Steps 3 and 4 and collect the  $I_i$  and  $D_i$  values at which Dens-ID outputs the  
183 pre-set  $\rho_{\text{mix}}$ . When the rainfall intensity  $I_i$  increases to  $I_{\max}$ , the calculation for a given AEP<sub>*i*</sub> is  
184 complete. Thus, the data set of  $I_i$  and  $D_i$  for a certain AEP<sub>*i*</sub> is obtained, and the corresponding  $ID$   
185 threshold curve can be fitted using these data.

186 Step 6: Repeat Steps 2, 3, 4, and 5, and collect the  $I_i$  and  $D_i$  values. When AEP reaches 120  
187 mm, the calculation for a given  $\rho_{\text{mix}}$  is complete.



188

189

Fig. 1 Flow chart of model calculation for obtaining  $[I, D]$  data

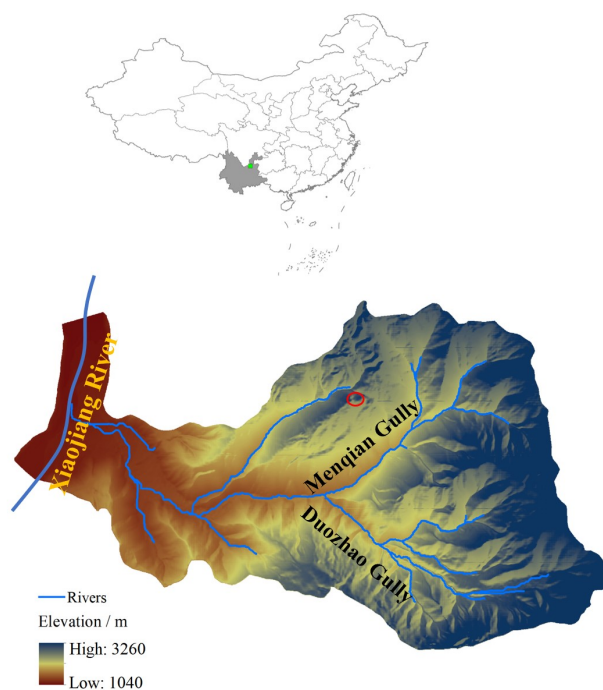
### 190 3 Study area and data collection

#### 191 3.1 Jiangjia Gully

192 JJG is located in the Dongchuan district of Kunming City, Yunnan Province, China, and is the  
 193 primary tributary of the Xiaojiang River. JJG has a drainage area of 48.6 km<sup>2</sup>, and its elevation  
 194 ranges from 1040 to 3260 m (Fig. 2). The terrain in JJG is steep; the relative relief between the  
 195 ridge and valley is approximately 500 m, and most slopes have a gradient exceeding 25°. Menqian



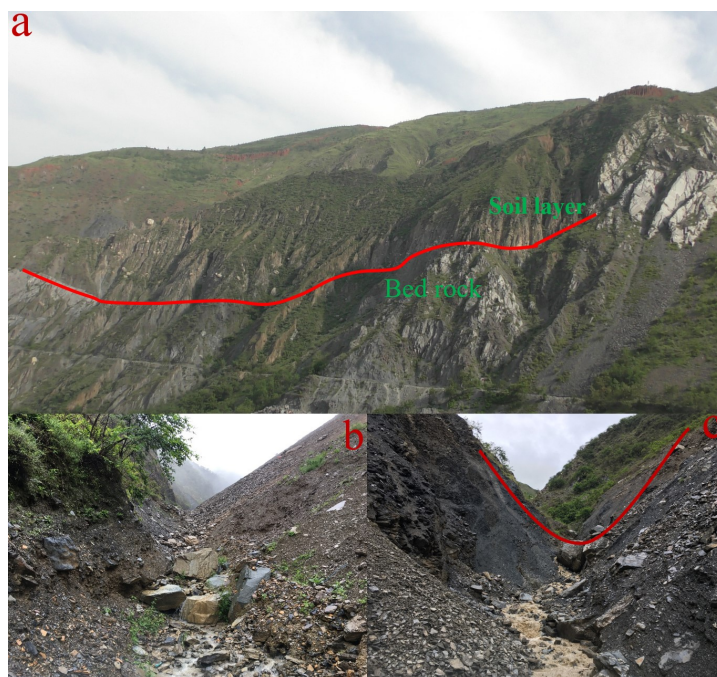
196 and Duozhao gullies, which are shown in Fig. 2, are the two main tributaries and account for  
197 64.7% of the entire drainage area. These two tributaries constitute the initiation zones of debris  
198 flow in JJG, and their channels are typically narrow and V-shaped [Fig. 3(c)]. JJG is characterized  
199 by intense tectonism, and approximately 80% of the exposed rocks are highly fractured and  
200 slightly metamorphosed. The predominant sandstone and slate can be easily identified by their  
201 light and dark colors, respectively. Both rock types are weak and easily weathered and fragmented  
202 (Yang et al., 2020).



203

204

Fig. 2 Location of JJG



205

206

Fig. 3 Loose solid material in JJG

207

The slopes on both sides of JJG are covered by a loose soil mass tens of meters in thickness

208

[Fig. 3(a)]. Because of intense rainfall, shallow landslides frequently occur on the slopes and

209

provide a large amount of loose solid material for debris flows [Fig. 3(b)]. The steep terrain and

210

large amount of loose solid material in JJG provide suitable conditions for debris flow formation.

211

According to the collected rainfall data, high-intensity or long-duration rainfall can trigger debris

212

flow events (Guo et al., 2013; Zhang et al., 2020). The solid material in JJG originates mainly

213

from shallow landslides, which is consistent with the model assumptions. Therefore, JJG is chosen

214

as the study area to quantitatively examine the effect of AEP on the *ID* threshold curves of debris

215

flows.

216

### 3.2 Data for model calculation and validation

217

◆ Terrain data



218 DEM data for JJG were provided by the Dongchuan Debris Flow Observation and Research  
219 Station. The spatial resolution of the DEM is 0.5 m, and the data were obtained in December 2017  
220 by aerial photogrammetry using an unmanned aerial vehicle. A DEM with a grid size of 10 m was  
221 generated from the original terrain data using the resampling tools in ArcGIS, which were used to  
222 derive the geometrical parameters of JJG such as slope length, gradient, and river channels.

223 ◆ Data necessary for hydrological simulation

224 Three main soil types (Table 1) occur in the JJG: dry red soil, red-yellow soil, and gravelly  
225 soil. Gravelly soil is widely distributed upstream in JJG and is the main source of solid material  
226 for debris flow. The hydrological parameters listed in Table 1 were obtained from the National  
227 Soil Database. The grid size of the land use map is 250 m, and its parameters, such as the  
228 normalized difference vegetation index, were obtained from the Moderate Resolution Imaging  
229 Spectroradiometer database. These data related to hydrological parameters were converted into a  
230 map with an accuracy comparable to that of the DEM using the resampling tool in ArcGIS.

231 Table 1 Soil types and their hydrological parameters

Soil type	$\theta_s$	$\theta_t$	Parameters of curve		$f_s$ (mm/h)
			$\alpha$	$n$	
Gravelly soil	0.54017	0.07639	0.02201	1.37785	30.486
Red-yellow soil	0.48519	0.06829	0.02264	1.38146	21.964
Dry red soil	0.48148	0.07640	0.01476	1.47394	10.811

232 ◆ Soil mechanical parameters

233 Eq. 7 (section 4.3) can be used to determine two soil mechanical parameters, soil cohesion  $c$   
234 and internal friction angle  $\varphi$ , by direct shear tests of soil samples from JJG. Most of the solid  
235 material for debris flows in JJG originates from gravelly soil; therefore, three groups of soil  
236 samples were taken from several typical slopes covered by a gravelly soil mass, and one sample  
237 each was taken from the red-yellow and dry red soil. As shown in Table 2, the three samples from



238 gravelly soils have similar  $c$  and  $\varphi$  values; therefore, the average values of the two parameters  
239 were calculated to represent the mechanical performance of the gravelly soil mass. The  
240 mechanical parameters in Table 2 can be assigned to each grid cell of the DEM according to the  
241 distribution of soil types in JJG.

242 Table 2 Cohesion  $c$  and internal friction angle  $\varphi$  of soil samples from JJG

Soil samples	Soil mechanical parameter			
	$c$ (kPa)	$\varphi$ (deg)	Average $c$ (kPa)	Average $\varphi$ (deg)
Gravelly soil-1	35.1	36.0	34.5	34.4
Gravelly soil-2	35.9	33.7		
Gravelly soil-3	32.5	33.7		
Red-yellow soil	27.0	36.3	27.0	36.3
Dry red soil	25.9	35.7	25.9	35.7

243 ◆ Historical debris flow and rainfall data

244 To validate the quantitative relationship between the AEP and the  $ID$  threshold curves of  
245 debris flows, data for 45 debris flow events in JJG and the triggering rainfall processes were  
246 collected. Rainfall events must be separated from long-term rainfall sequences to identify the  
247 rainfall processes that triggered the 45 debris flow events. The inter-event time (IET) was defined  
248 as a measure of the minimum time interval between two consecutive rainfall pulses (Adams et al.,  
249 1986). Although the IET strongly affects the start and end times of an event (Bel et al., 2017),  
250 there are no standard criteria for rainfall episode separation (Jiang et al., 2021). Peres et al. (2018)  
251 noted that the IET depends on whether the rainfall during an IET is smaller than the mean daily  
252 potential evapotranspiration (MDPE). Long-term observation of the evaporation in JJG showed  
253 that the MDPE in this gully is approximately 4 mm; thus, precipitation of less than 0.5 mm during  
254 an IET is considered to indicate the end of a rainfall process.



255 The AEP was calculated as the weighted sum of rainfall periods before a debris flow (Long et  
 256 al., 2020) and is expressed as follows:

$$257 \quad AEP = \sum_{i=1}^n K^n R_i \quad (6)$$

258 where the AEP is the antecedent effective rainfall;  $K$  is the attenuation coefficient, which is equal  
 259 to 0.78 according to a field test in JJG (Cui et al., 2003); and  $n$  is the number of days preceding the  
 260 debris flow. Table 3 lists the calculated AEP, average rainfall intensity ( $I$ ), and rainfall duration ( $D$ )  
 261 of each debris event. The calculated AEP values in the third column of Table 3 are rounded to  
 262 integers to increase the number of debris flow events corresponding to each AEP. AEP values of  
 263 90 and 60 mm are associated with 1 debris flow event each, 8 events have an AEP value of 40 mm,  
 264 13 events have an AEP value of 30 mm, 14 events have an AEP value of 20 mm, and 8 events  
 265 have an AEP value of 15 mm.

266 Table 3 Historical data of debris flow events and rainfall

Number	Date	AEP	Rounded AEP	Rainfall duration (h)	Intensity (mm/h)
1	2004/7/9	92.60	90	9.30	1.00
2	2001/6/29	59.30	60	4.50	6.70
3	2008/7/5	44.77	40	8.88	1.97
4	2001/7/4	42.50		21.7	1.40
5	2001/7/8	39.80		6.8	3.80
6	2008/8/7	39.73		27.10	1.58
7	2008/6/15	38.87		16.90	1.43
8	2007/7/24	38.35		6.05	2.89
9	1999/8/25	36.20		7.8	3.10
10	2006/7/6	35.20		2.27	10.37
11	1999/7/16	34.00	30	4	11.8



12	2008/7/21	33.47		10.43	2.65
13	2000/8/9	31.60		2.3	8.6
14	2008/8/3	31.35		7.25	3.14
15	2010/7/17	30.385		1.00	4.6
16	2001/6/27	30.30		4	13.1
17	2007/9/17	30.15		9.38	2.44
18	2001/8/13	29.80		3.2	5.3
19	1994/6/26	29.00		2	23
20	2008/7/31	28.99		6.93	2.18
21	1999/7/24	28.90		4.8	9.80
22	2001/8/22	28.00		3.50	6.00
23	2008/8/17	26.29		3.75	3.23
24	2006/8/20	24.63		3.15	2.32
25	1999/8/10	23.60		14.20	4.30
26	2000/8/8	23.50		5.20	8.50
27	2008/7/1	23.22		9.88	2.60
28	2000/8/29	22.70		6.00	6.20
29	2010/7/6	22.376		10.88	4.18
30	2008/7/11	21.33	20	1.85	6.43
31	2006/8/15	20.62		3.08	9.79
32	2006/7/5	20.52		2.32	10.53
33	2000/7/15	19.60		26.2	2.90
34	1993/8/29	18.60		6.70	4.60
35	1998/8/2	18.40		3.70	7.30
36	2004/6/26	18.10		3.50	5.00
37	2007/8/24	16.69		28.60	1.77
38	2007/8/11	14.63	15	6.80	1.88
39	2007/7/10	14.40		1.48	7.01





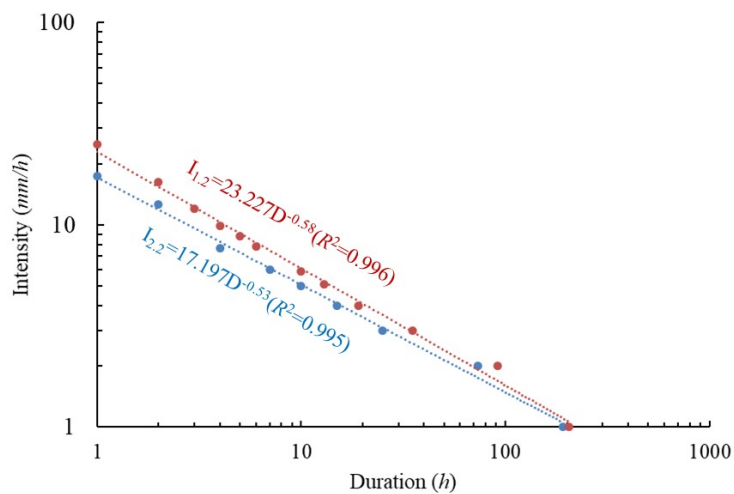
40	2001/6/26	13.40		3.90	11.80
41	2004/7/19	12.60		2.00	9.80
42	1994/6/15	12.50		8.70	6.10
43	1993/8/26	12.10		8.7	3.60
44	2009/8/4	11.90		5.72	9.34
45	2010/9/10	11.51		6.03	5.55

267

## 268 4 Results and Discussion

### 269 4.1 *ID* threshold curves of debris flow with different AEP

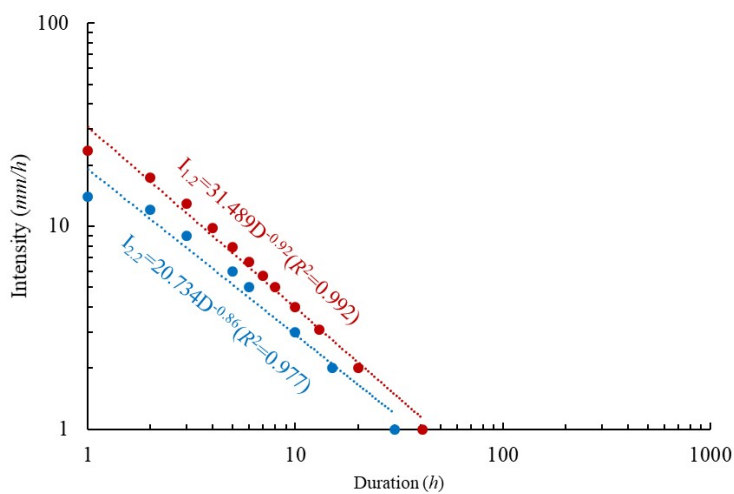
270 Fig. 4 shows three sets of *ID* threshold curves for debris flows with AEP values of 20, 60,  
271 and 10 mm. All of the axes are given on a logarithmic scale. As shown in Fig. 4(a) (AEP = 20  
272 mm), two *ID* threshold curves corresponding to  $\rho_{mix} = 1.2$  and  $\rho_{mix} = 2.2$  g/cm<sup>3</sup> constitute the  
273 boundaries of the rainfall threshold that triggers debris flow in JJG. The *ID* threshold curves in Fig.  
274 4 can be described by a power function; this result is consistent with the shape of the threshold  
275 curve obtained by the statistical model, indicating that our model can describe the hydrological  
276 process of rainfall-induced debris flow. The *ID* threshold curve corresponding to a density of 2.2  
277 g/cm<sup>3</sup> is located below the curve that corresponds to a density of 1.2 g/cm<sup>3</sup>, indicating that debris  
278 flows with higher density are more easily triggered in JJG. AEP has a significant qualitative effect  
279 on the *ID* threshold curve of a debris flow. Essentially, a large AEP value indicates that the rainfall  
280 requirements for rainfall-induced debris flow are low. For  $D = 1$  h, the rainfall intensity  $I$  that can  
281 trigger a debris flow with a density of 1.2 g/cm<sup>3</sup> decreases from 26.2 to 16.7 mm/h with increasing  
282 AEP. The trend revealed by this calculation result is essentially consistent with the results of field  
283 observations in JJG (Cui et al., 2003).



284

285

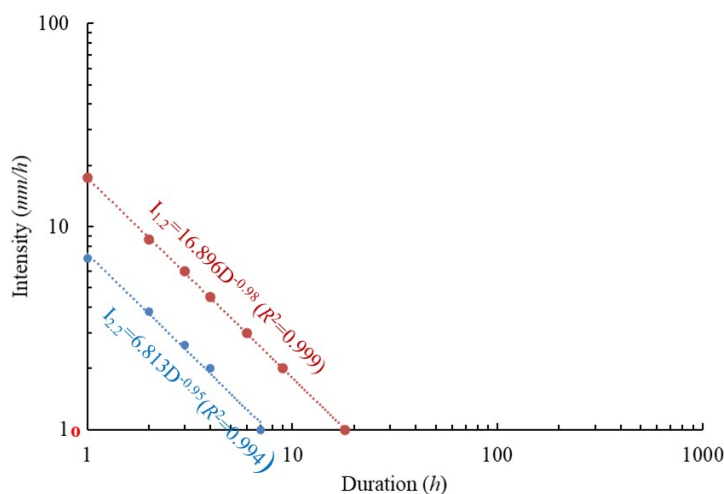
(a) AEP = 20 mm



286

287

(b) AEP = 60 mm



(c) AEP = 100 mm

Fig. 4 ID threshold curves of debris flow for different AEP values

288

289

290

291

292

293

294

295

In addition, Fig. 4 shows that the distance between the two ID threshold curves becomes larger with increasing AEP, indicating a higher occurrence probability of rainfall-induced debris flow. A database including all the data sets, including  $[I, D]$ , the fitted curves, and AEP (Table 4) was used to quantitatively analyze the effect of AEP on the threshold curve.

Table 4 Database of AEP, fitted equations, and  $[I, D]$  data groups

AEP (mm)	Fitted threshold curves of debris flow in JJG	
	1.2 g/cm <sup>3</sup>	2.2 g/cm <sup>3</sup>
10	$I_{1,2} = 19.851D^{-0.54} D \in [1, 269] (R^2 = 0.991)$	-
15	$I_{1,2} = 21.69D^{-0.55} D \in [1, 236] (R^2 = 0.993)$	$I_{2,2} = 16.10D^{-0.50} D \in [1, 229] (R^2 = 0.995)$
20	$I_{1,2} = 23.227D^{-0.58} D \in [1, 203] (R^2 = 0.996)$	$I_{2,2} = 17.197D^{-0.531} D \in [1, 192] (R^2 = 0.995)$
30	$I_{1,2} = 26.24D^{-0.64} D \in [1, 143] (R^2 = 0.996)$	$I_{2,2} = 18.087D^{-0.57} D \in [1, 132] (R^2 = 0.995)$
40	$I_{1,2} = 40.589D^{-0.78} D \in [1, 103] (R^2 = 0.966)$	$I_{2,2} = 22.154D^{-0.64} D \in [1, 92] (R^2 = 0.984)$
50	$I_{1,2} = 41.263D^{-0.86} D \in [1, 65] (R^2 = 0.981)$	$I_{2,2} = 23.501D^{-0.74} D \in [1, 55] (R^2 = 0.980)$
60	$I_{1,2} = 31.489D^{-0.92} D \in [1, 40] (R^2 = 0.992)$	$I_{2,2} = 20.734D^{-0.86} D \in [1, 30] (R^2 = 0.977)$

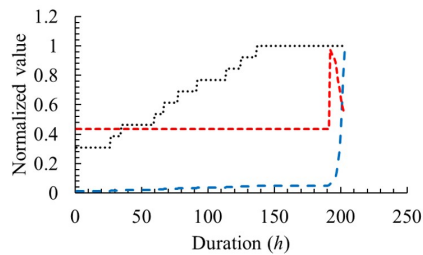


70	$I_{1.2} = 23.049D^{-0.96} D \in [1, 25] (R^2 = 0.9983)$	$I_{2.2} = 13.042D^{-0.93} D \in [1, 15] (R^2 = 0.995)$
80	$I_{1.2} = 18.719D^{-0.98} D \in [1, 20] (R^2 = 0.997)$	$I_{2.2} = 9.960D^{-0.95} D \in [1, 11] (R^2 = 0.999)$
90	$I_{1.2} = 16.991D^{-0.98} D \in [1, 18] (R^2 = 0.999)$	$I_{2.2} = 6.813D^{-0.95} D \in [1, 7] (R^2 = 0.994)$
100	$I_{1.2} = 16.896D^{-0.98} D \in [1, 18] (R^2 = 0.999)$	$I_{2.2} = 6.813D^{-0.95} D \in [1, 7] (R^2 = 0.994)$
110	$I_{1.2} = 16.873D^{-0.98} D \in [1, 16] (R^2 = 0.999)$	$I_{2.2} = 6.755D^{-0.95} D \in [1, 7] (R^2 = 0.997)$
120	$I_{1.2} = 16.873D^{-0.98} D \in [1, 16] (R^2 = 0.999)$	$I_{2.2} = 6.755D^{-0.95} D \in [1, 7] (R^2 = 0.997)$

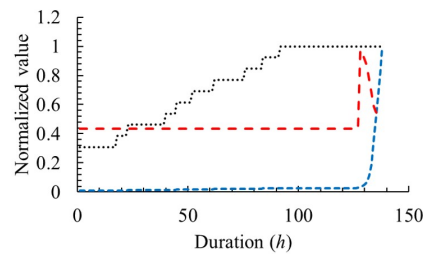
296 Note that Dens-ID cannot collect sufficient  $[I_i, D_i]$  data for fitting the  $ID$  threshold curve for a  
 297 density of  $2.2 \text{ g/cm}^3$  and  $AEP = 10 \text{ mm}$ . At this low  $AEP$  value, the supply rate of solid material is  
 298 lower than the runoff rate; thus, it is difficult to trigger a high-density debris flow in JJG. By  
 299 contrast, for  $AEP \geq 90 \text{ mm}$ ,  $\alpha$  and  $\beta$  tend to be constant. The  $AEP$  can significantly affect the  $ID$   
 300 curves of debris flow in JJG at values of 10 to 90 mm.

#### 301 4.2 Effects of loose solid material and runoff on debris flow formation

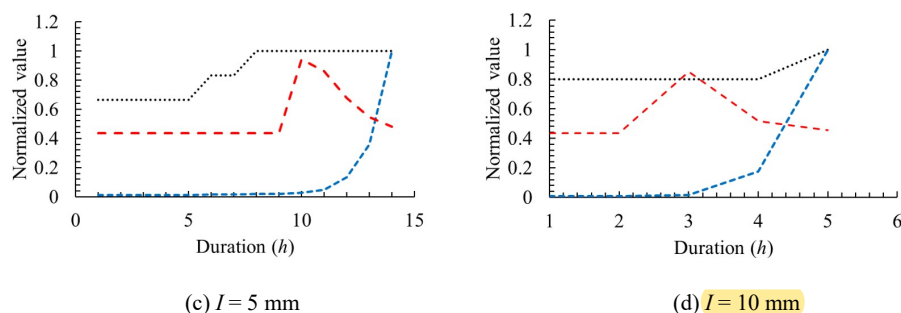
302 In Dens-ID, the parameters  $V_w(t)$  and  $V_s(t)$  in Eq. 1 are the process variables for calculating  
 303 the density of the water-soil mixture. Because the  $ID$  threshold curves in Fig. 4 are all related to  
 304 the debris flow density, it is necessary to analyze the relationship between debris flow density and  
 305  $V_w(t)$  and  $V_s(t)$  under different rainfall conditions.



306 (a)  $I = 1 \text{ mm}$



307 (b)  $I = 1.5 \text{ mm}$



310 Fig. 5 Process graphs of  $V_s(t)$ ,  $V_w(t)$ , and  $\rho_{mix}(t)$  for different rainfall intensity values  $I$  and AEP = 20 mm.

311 Black dotted line represents the volume variation of  $V_s(t)$ , blue dotted line represents the volume variation of

312  $V_w(t)$ , and red dotted line represents the density of the water-soil mixture.

313 Fig. 5 shows process graphs of  $V_s(t)$ ,  $V_w(t)$ , and  $\rho_{mix}(t)$  for different rainfall intensity  
314 values  $I$  at AEP = 20 mm. Because these three parameters have different magnitudes, they were  
315 normalized to better show their dynamic evolution.

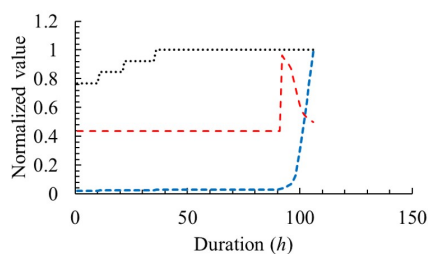
316 The red curve represents the debris flow density for different rainfall intensity values  $I$ , which  
317 reveals a clear water process (Stage 1), debris flow phase (Stage 2), and hyperconcentrated flow  
318 stage (Stage 3). In Stage 1, the runoff rate is lower than the supply rate of solid material (black  
319 dotted line) in JJG. During this stage, the runoff in JJG cannot provide hydrodynamic conditions  
320 suitable for transporting these loose deposits, and no debris flow occurs. In Stage 2, during  
321 continuous hydrological processes such as rainfall infiltration and runoff generation, the total  
322 volume of runoff ( $V_w(t)$ ) in JJG increases rapidly, and the blue dotted lines in Fig. 5(a)–(d), which  
323 represent the volume variation of  $V_w(t)$ , all show a sharp increase. Consequently, the  
324 hydrodynamic conditions are sufficient for debris flow formation. The rainfall-induced loose solid  
325 material and runoff in the channel can be fully coupled, and thus a debris flow can be triggered. In  
326 Stage 3, a sudden increase in runoff volume and decrease in the supply rate of loose solid material



327 cause the debris flow in JJG to quickly become hyperconcentrated. Therefore, the red dotted line  
328 in Fig. 5 also shows that debris flows generally begin suddenly but quickly reach Stage 3 because  
329 of the rapid increase in runoff.

330 The black dashed line in Fig. 5 represents the variation of  $V_s(t)$ . The hydrological conditions  
331 represented by AEP = 20 mm induce shallow landslides in JJG before rainfall begins. In the initial  
332 stage of the rainfall process, the supply rate of solid material is higher than the runoff rate in JJG;  
333 however, as the rainfall process continues, the supply rate is overtaken by the runoff rate, and the  
334 total volume stabilizes at a maximum value.

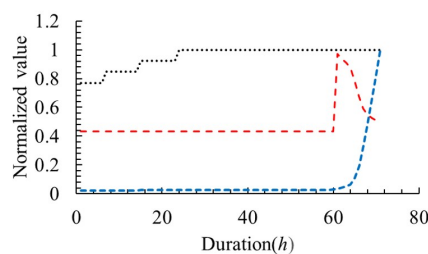
335 The blue dashed lines in Fig. 5 represent the variation of  $V_w(t)$ . They all show a sharp  
336 increase at a certain time, at which debris flows also occur. Thus, the sudden occurrence of debris  
337 flows is caused mainly by increasing runoff. These results indicate that the supply of loose solid  
338 material is essential to debris flow formation, but the decisive factor in debris flow occurrence is  
339 the sharp increase in runoff.



340

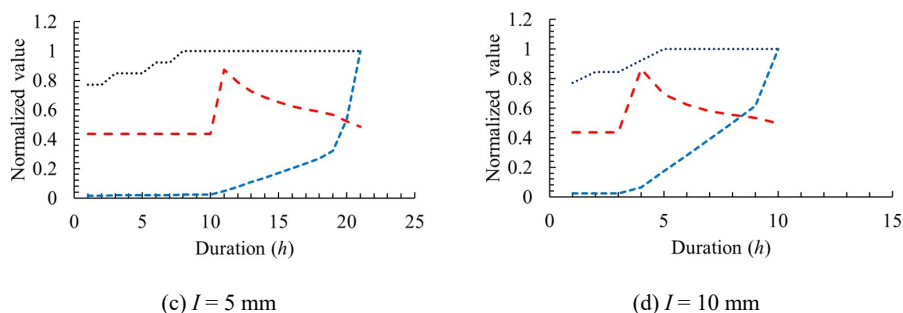
(a)  $I = 1 \text{ mm}$

341



(b)  $I = 1.5 \text{ mm}$

342



343

344

345

346

347

348

349

350

351

352

353

354

355

356

357

358

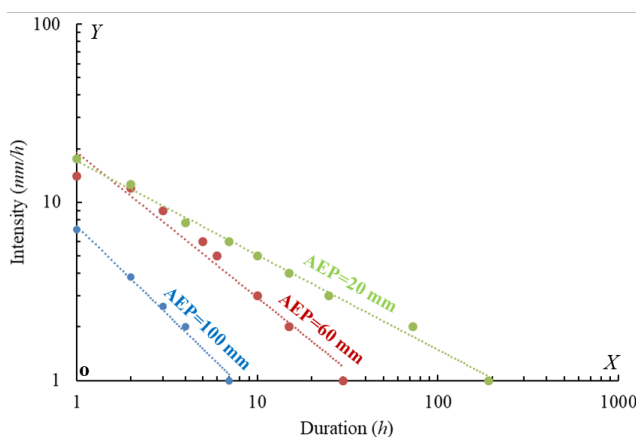
Fig. 6 Process graphs of  $V_s(t)$ ,  $V_w(t)$ , and  $\rho_{mix}(t)$  for different rainfall intensity values  $I$  and AEP = 40 mm.

Black dotted line represents the volume variation of  $V_s(t)$ , blue dotted line represents the volume variation of

$V_w(t)$ , and red dotted line represents the density of the water-soil mixture.

#### 4.3 Quantitative analysis of effects of AEP on $\alpha$ and $\beta$

The three  $ID$  curves from Fig. 4 corresponding to a density of  $2.2 \text{ g/cm}^3$  and different AEP values are plotted in Fig. 7 to further examine the variation of the  $ID$  curves with AEP. The AEP can change the position of the  $ID$  threshold curve in the  $I$ - $D$  coordinate system, indicating that a higher AEP value shifts the  $ID$  threshold curve closer to the origin. This tendency is consistent with the general consensus that higher AEP can decrease the triggering rainfall conditions (De Vita et al., 2000; Cui et al., 2003; Bel et al., 2017). Consequently, considering the landslide-dominated solid resource supply in JJG, Dens-ID describes the formation process of rainfall-induced debris flow reasonably well. In addition, compared to the range of rainfall intensity  $I$  ( $Y$  axis), the rainfall duration  $D$  ( $X$  axis) changes more dramatically with AEP and can quickly decrease from 192 h (AEP = 20 mm) to 7 h (AEP = 100 mm).



359

360 Fig. 7  $ID$  curves corresponding to a density of  $2.2 \text{ g/cm}^3$  and AEP values of 20, 60, and 100 mm

361 The parameters of the  $ID$  threshold curve of debris flow,  $\alpha$  and  $\beta$ , determine the position of  
 362 the fitting curve in  $I$ - $D$  coordinates. Therefore, it can be deduced that  $\alpha$  and  $\beta$  depend on AEP. In  
 363 this section, the data sets from Dens-ID are used to derive the functional relationships between  
 364 AEP and these two parameters. First, it is necessary to clarify the physical meaning of  $\alpha$  and  $\beta$ .  
 365 Under the numerical simulation conditions of this study, the variation interval of the independent  
 366 variable  $D$  in the formula  $I = \alpha D^\beta$  is  $[1, D_{\max}]$ , and the variation interval of  $I$  is  $[I_{\max}, 1]$ . According  
 367 to the formula, when  $D$  is equal to 1 h,  $I = \alpha$ . When  $D = 1$ , the rainfall duration required to trigger  
 368 a debris flow is 1 h, and the rainfall intensity  $I$  reaches the maximum value,  $I_{\max}$ . Therefore, the  
 369 combination of  $D$  and  $I$  under these conditions represents high-intensity rainfall. According to this  
 370 analysis,  $\alpha$  is numerically equal to the value of  $I_{\max}$ , and thus this parameter represents the critical  
 371 rainfall intensity required to trigger a debris flow for  $D = 1$  h.

372 Before the physical meaning of  $\beta$  is discussed, the expression  $I = \alpha D^\beta$  needs to be written  
 373 logarithmically, as follows:

$$374 \quad \log I = \log \alpha + \beta \log D \quad (7)$$

375 By denoting  $\log I$  as  $Y_I$ ,  $\log D$  as  $X_D$ , and  $\log \alpha$  as  $B_\alpha$ , Eq. 7 can be rewritten as follows:





376 
$$Y_I = \beta X_D + B_\alpha \quad (8)$$

377  $X_D$  and  $Y_I$  are related to  $I$  and  $D$  and are independent variables with ranges of  $[\log 1, \log(D_{\max})]$

378 and  $[\log 1, \log(I_{\max})]$ , respectively. The rewritten equation is represented by a linear equation in

379 Figs. 4 and 5, where  $\beta$  is the slope of each line and is less than 0. The main reason that  $\beta$  is less

380 than 0 is a tradeoff between rainfall intensity and rainfall duration in nature, which facilitates the

381 occurrence of debris flow. The absolute value of  $\beta$  represents the deceleration rate of rainfall

382 intensity with increasing rainfall duration, that is, the rate of decrease from  $I_{\max}$  to 1 mm/h. The  $\alpha$

383 and  $\beta$  values in Table 4 can be classified into two groups according to debris flow density (1.2 or

384 2.2 g/cm<sup>3</sup>). The  $\alpha$  and  $\beta$  values in the two groups show similar variation with AEP. Thus, one data

385 group (Table 5) corresponding to a density of 2.2 g/cm<sup>3</sup> was selected to examine the effect of AEP

386 on  $\alpha$  and  $\beta$ .

387 Table 5 Calculated  $\alpha$  and  $\beta$  for different AEP values

Fitting parameter	AEP (mm)											
	10	20	30	40	50	60	70	80	90	100	110	120
$\alpha$	-	17.2	18.1	22.2	23.5	20.7	13.0	9.9	6.8	6.8	6.8	6.8
$\beta$	-	-0.53	-0.57	-0.64	-0.74	-0.86	-0.93	-0.95	-0.95	-0.95	-0.95	-0.95

388 **Effect of AEP on  $\alpha$ :** The effect of AEP on  $\alpha$  is described by the following equations, which

389 were fitted using the AEP and  $\alpha$  values in Table 5:

390 
$$\begin{cases} \alpha = -0.0078AEP^2 + 0.68AEP + 6.43 & 20 \leq AEP < 90 \\ \alpha = 6.8 & 90 \leq AEP \leq 120 \end{cases} \quad (9)$$

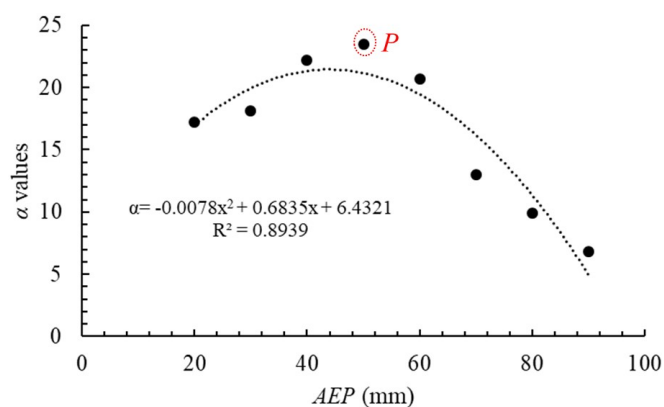
391 The condition for  $\alpha = I_{\max}$  is  $D = 1$ , and the combination of  $D = 1$  and  $\alpha$  represents a high-

392 intensity, short-duration rainfall process. As shown in Fig. 8, Eq. 9 is used to quantify the rainfall

393 intensity threshold at which this type of rainfall process triggers a debris flow for different AEP



394 values. In Fig. 8,  $\alpha$  (or  $I_{\max}$ ) represents parabolic variation with AEP. Interestingly,  $\alpha$  does not  
395 always decrease with continuously increasing AEP. When  $AEP \leq 50$  mm, the  $\alpha$  values necessary  
396 for triggering a debris flow increase simultaneously with AEP; when  $AEP > 50$  mm,  $\alpha$  decreases  
397 with increasing AEP, but the decrease does not continue indefinitely with increasing AEP, because  
398 for  $AEP > 90$  mm,  $\alpha$  is constant at 6.8 mm (Table 5).



399

400

Fig. 8 Function curve describing the relationship between AEP and  $\alpha$

401

The key variables  $V_s$  and  $V_w$  are used to explain the quantitative evolution described by Eq. 9.

402

To facilitate the analysis, the  $V_s$  and  $\alpha$  values calculated by Dens-ID were normalized, and they are

403

plotted versus AEP (AEP- $V_s$  and AEP- $\alpha$ ) in Fig. 9.  $V_s$  increases continuously for  $AEP < 50$  mm,

404

at which it reaches a maximum. As  $V_s$  increases with increasing AEP, a larger volume value of

405

runoff ( $V_w$ ) is required to bring the debris flow density ( $\rho_{mix}$ ) to a fixed value of 2.2 or 1.2 g/cm<sup>3</sup>,

406

which requires stronger hydrodynamic conditions, and thus a higher hourly rainfall intensity.

407

Before point P<sub>1</sub> in Fig. 9, the rainfall intensity (or  $\alpha$ ) at which a debris flow occurs for  $D = 1$  is

408

positively correlated with AEP. Although AEP no longer contributes to the variation of  $V_s$  after

409

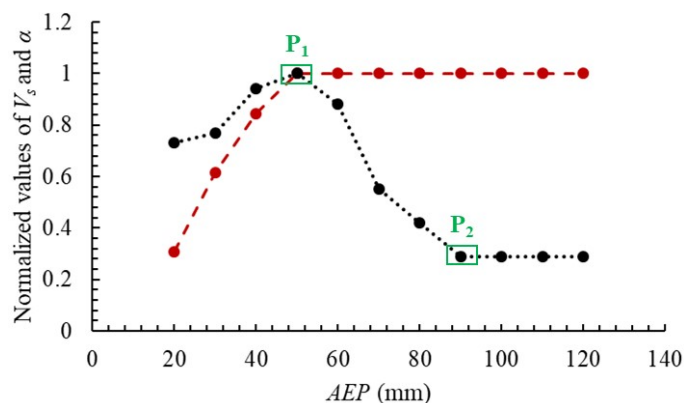
AEP reaches 50 mm, the soil water content can still increase with continuously increasing AEP,

410

reducing the surface infiltration rate and increasing the runoff volume generated from rainfall.



411 Under these hydrological conditions, the rainfall intensity  $I_{\max}$  (or  $\alpha$ ) required to trigger a debris  
 412 flow with a fixed density value decreases gradually; thus,  $\alpha$  is negatively correlated with AEP.  
 413 When AEP exceeds 90 mm ( $P_2$  in Fig. 9),  $\alpha$  stops gradually decreasing and remains constant,  
 414 indicating that at AEP = 90 mm, the loose solid material in JJG become saturated. Under these  
 415 hydrological conditions,  $\alpha$  has a constant value of 6.8 mm and does not change with AEP.  
 416 Therefore, for the two inflection points  $P_1$  and  $P_2$  in Fig. 9, AEP is the external driving factor and  
 417 operates through the entire process of debris flow formation in JJG, whereas the limiting  
 418 conditions, maximum  $V_s$  and constant saturated soil water content ( $\theta_s$ ), are the two intrinsic factors.



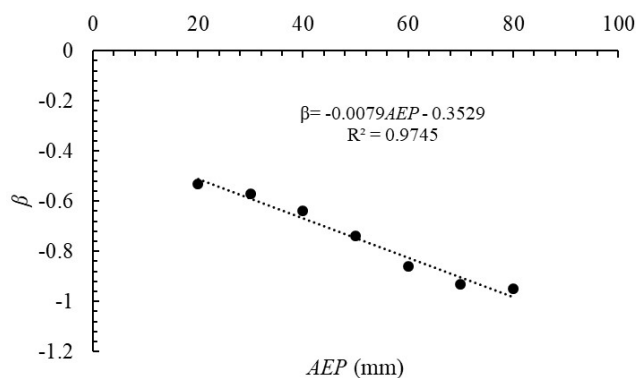
419  
 420 Fig. 9 AEP- $\alpha$  curve (black dashed line) and AEP- $V_s$  curve (red dashed line)

421 **Effect of AEP on  $\beta$ :** The effect of AEP on  $\beta$  is described by the following equations, which  
 422 were fitted using the AEP and  $\beta$  values in Table 5.

423

$$\begin{cases} \beta = -0.0079AEP - 0.35 & 20 \leq AEP < 90 \\ \beta = -0.95 & 90 \leq AEP \leq 120 \end{cases} \quad (10)$$

424



425

426 Fig. 10 Function curve describing the relationship between AEP and  $\beta$  for AEP values ranging from 20 to 90 mm

427 Eq. 10 and Fig. 10 show that as AEP increases from 20 to 90 mm,  $\beta$  decreases linearly. When

428 AEP exceeds 90 mm,  $\beta$  becomes a constant with a value of  $-0.95$ . These results, in combination

429 with Eq. 9, reveal that  $\alpha$  and  $\beta$  in the  $ID$  threshold equation are constant when AEP exceeds 90

430 mm. This result further shows that there is an interval in which AEP affects the  $ID$  threshold curve

431 of debris flow in JJG, specifically,  $AEP \in [20,90]$ .

#### 432 4.4 Validation of quantitative relationship

433 Using the historical rainfall data in Table 3, four  $ID$  threshold curves for different AEP values

434 were fitted, as shown Fig. 11. The green dotted line represents  $AEP = 15$  mm, and the fitted

435 equation is  $I = 11.99D^{-0.45}$ . The red dotted line represents  $AEP = 20$  mm ( $I = 10.58D^{-0.44}$ ). The

436 black dotted line represents  $AEP = 30$  mm ( $I = 13.16D^{-0.60}$ ). The orange dotted line represents

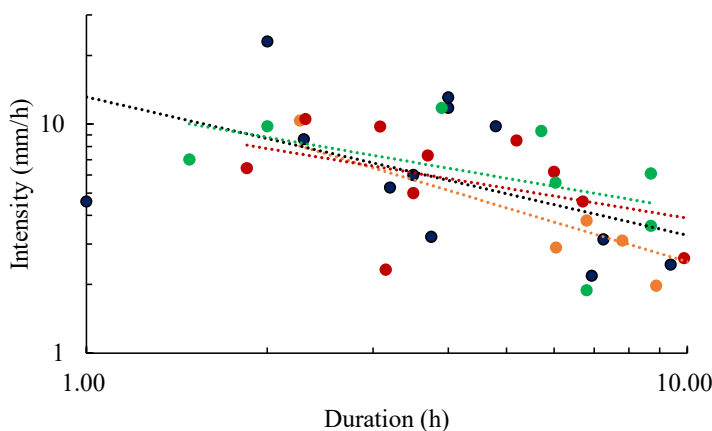
437  $AEP = 50$  mm ( $I = 15.25D^{-0.78}$ ). These lines differ when  $D$  is larger than 3. For  $D > 3$ , the  $ID$

438 threshold curve appears lower in the  $I-D$  coordinate system with increasing AEP, indicating that

439 lower rainfall conditions will trigger debris flow. This tendency is consistent with the simulated

440 results in Fig. 7, further demonstrating that Dens-ID may be able to describe the formation process

441 of rainfall-induced debris flow.



442  
443 Fig. 11 Historical-data-based  $ID$  curves for different AEP values. Green, red, black, and orange symbols and lines  
444 represent AEP values of 15, 20, 30, and 50, respectively.

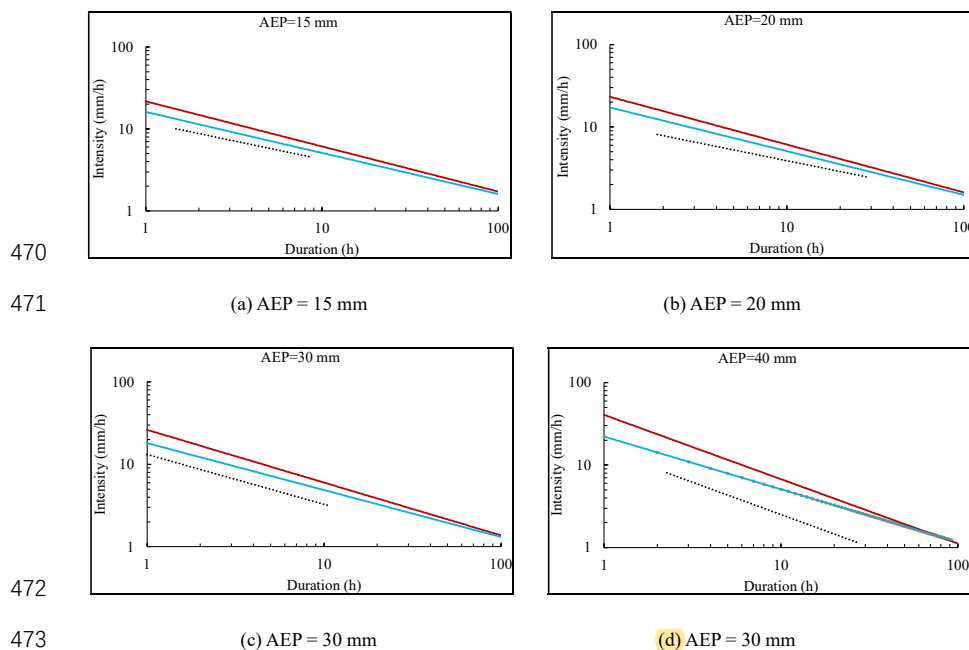
445 The curves fitted using historical rainfall data and Dens-ID for the same AEP were drawn in  
446 separate graphs, where each graph corresponds to a different AEP value between 15 and 90 mm.

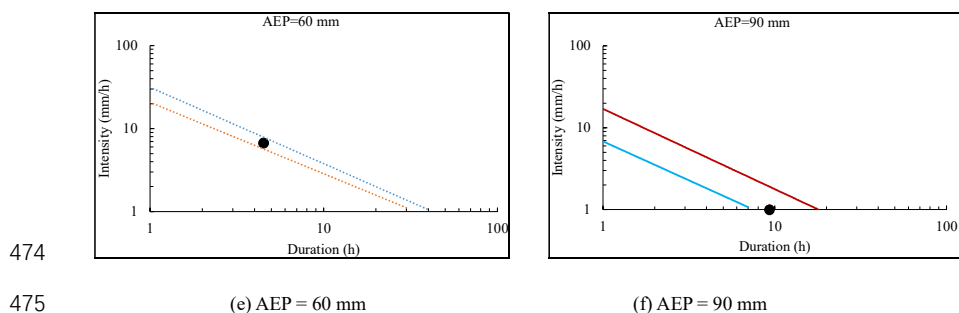
447 As shown in Table 2, only one debris flow event each was collected from the observation station  
448 for AEP values of 60 and 90 mm. In Fig. 12(e) and (f), the single points at which the  $I$  and  $D$  data  
449 in Table 3 coincide with the model-derived curves are indicated. These points are located between  
450 the threshold curves, which are isodensity curves corresponding to debris flow densities of 2.2 and  
451 1.2  $\text{g}/\text{cm}^3$ . Any combination of  $I$  and  $D$  between these two isodensity curves indicates that these  
452 rainfall conditions can trigger a debris flow. Because the closed area formed by the two curves  
453 covers historical data on rainfall that triggered a debris flow event, the curves derived by Dens-ID  
454 are at reasonable positions in  $I$ - $D$  coordinates (that is, the  $\alpha$  and  $\beta$  values that determine the  
455 position of  $I = \alpha D^\beta$  in  $I$ - $D$  coordinates are reasonable). Therefore, the  $\alpha$  and  $\beta$  values of the Dens-  
456 ID-derived threshold curves corresponding to AEP values of 60 and 90 mm can be used to analyze  
457 the relationship between AEP and  $\alpha$  and  $\beta$ .

458 Forty-three debris flow events corresponding to AEP values of 15, 20, 30, and 40 mm are



459 plotted in Fig. 12(a)–(d). Four  $ID$  threshold curves (black dashed lines) corresponding to these  
460 AEP values were fitted using the rainfall data associated with each event. In each panel, the red  
461 and blue lines are  $ID$  threshold curves fitted by Dens-ID for debris flow densities of  $1.2 \text{ g/cm}^3$  (the  
462 upper boundary for identifying debris flow formation) and  $2.2 \text{ g/cm}^3$  (the lower boundary),  
463 respectively (Zhang et al., 2020). If a data point representing  $(I, D)$  is above the black dashed or  
464 blue line, these rainfall conditions may trigger debris flows (Cain, 1980; Zhang et al., 2020).  
465 Although the black dashed and blue lines were fitted by different methods, both are used as lower  
466 limits for identifying debris flow formation. By using the black dashed line as a reference, the blue  
467 line can be calibrated according to its deviation from the black dashed line for each AEP value;  
468 then the errors of the equations describing the relationships between AEP and  $\alpha$  and  $\beta$  (Eqs. 9 and  
469 10, respectively) can be evaluated.





476 Fig. 12  $ID$  threshold curves fitted using historical data in Table 3 (black dashed line and Dens-ID (blue and red  
 477 lines)

478 As shown in Table 6, the errors of  $\alpha$  for AEP values of 40, 30, 20, and 15 mm are 39.1%, 50.1%,  
 479 27.1%, and 35.1%, respectively, and the average error is approximately 37.85%. The errors of  $\beta$   
 480 for AEP values of 40, 30, 20, and 15 mm are 14.6%, 21.7%, 2.30%, and 5.80%, respectively, and  
 481 the average error is approximately 11.10%. According to the physical meaning of  $\alpha$  and  $\beta$ , the  
 482 error of Eq. 9 (approximately 37.85%) indicates that Dens-ID overestimates the triggering rainfall  
 483 intensity ( $I_{\max}$ ) for  $D = 1$ . Additionally, the calculated  $\beta$  values, which represent the deceleration  
 484 rate of rainfall intensity with increasing rainfall duration, have a smaller error than the  $\alpha$  values.

485 Table 6 Error calibration using historical data

AEP (mm)	Fitted by historical data		Fitted by Dens-ID		Error (%)	
	$\alpha$	$\beta$	$\alpha$	$\beta$	$\alpha$	$\beta$
40	15.2	-0.78	21.15	-0.666	39.1	14.6
30	13.2	-0.6	19.81	-0.587	50.1	21.7
20	13.3	-0.52	16.91	-0.508	27.1	2.3
15	12	-0.45	14.875	-0.4685	35.1	5.8

486 The threshold curves fitted using historical rainfall data are below the Dens-ID fitting curves in  $I$ -



487  $D$  coordinates for the following reasons. (1) The process of debris flow formation in the gully is  
488 extremely complex, but Dens-ID cannot fully describe this process because of necessary  
489 simplifications in the code. Consequently, the simulated data may differ from the observed rainfall  
490 data, especially the triggering rainfall intensity ( $I_{\max}$  or  $\alpha$ ) for  $D = 1$ . (2) According to Zhang et al.  
491 (2020, 2021), Dens-ID is sensitive to input parameters such as rainfall, hydrology parameters, and  
492 soil mechanical parameters, and it is most sensitive to soil cohesion. Unavoidable uncertainties in  
493 many input parameters for the physical model can significantly affect the calculation results of  
494 Dens-ID (Raia et al., 2014; Zhang et al., 2018; Jacobs et al., 2020). (3) Local heavy rainfall in JJG  
495 is the main trigger for debris flow. The historical rainfall data in Table 3 were obtained at the  
496 rainfall station represented by a red circle in Fig. 2, which is approximately 2 km from Menqian  
497 Gully. Because of this spatial deviation, the rain gauge may be unable to detect the center of  
498 rainstorms, and thus the measured rainfall data may be smaller than the actual values.

## 499 5 Conclusions

500 Rainfall simulations using Dens-ID were employed to construct a database of  $ID$  threshold  
501 curves under different AEP conditions, and this database was used to thoroughly examine the  
502 quantitative effect of AEP on the  $ID$  threshold curves. The following conclusions are drawn.

503 (1) The  $ID$  threshold curve obtained using Dens-ID can be expressed by a power function,  
504 and the  $R^2$  values of the fitted power functions are all larger than 96%. The fitted curves from our  
505 model are all consistent in shape with the threshold curve obtained from the statistical model,  
506 indicating that the model can reflect the hydrological process of rainfall-induced debris flow with  
507 high reliability.

508 (2) The relationships between AEP and the parameters  $\alpha$  and  $\beta$  can be described by





509 functions that were verified using the *ID* curves fitted using historical rainfall data for JJG. The  
510 errors of the relationships between AEP and  $\alpha$  and  $\beta$  are approximately 37.85% and 11.10%,  
511 respectively. That is, Dens-ID overestimates the effects of AEP on  $\alpha$  and  $\beta$  compared to those  
512 indicated by historical rainfall data. This result can be attributed to limitations on the ability of  
513 Dens-ID to describe debris flow formation, the uncertainty of the input parameters of Dens-ID,  
514 and the suitability of rain gauge data for detecting rainstorm centers.

515 (3) The two derived equations can clarify the variation of debris flow *ID* curves with AEP.  
516 The conventional *ID* threshold curve remains the same regardless of AEP once it is determined.  
517 However, the AEP can significantly affect the determination of the *ID* curve. The effects of AEP  
518 on  $\alpha$  and  $\beta$  cause the originally static *ID* curve to become a variable threshold in the *I-D*  
519 coordinate system. Consequently, the *ID* curves fully reflect the effects of AEP when they are used  
520 to predict debris flow. Our study may improve the prediction precision of *ID* curves.

#### 521 **Acknowledgement:**

522 This work was supported by the National Key Research and Development Program of China  
523 (2018YFC1505503), Project of the Department of Science and Technology of Sichuan Province  
524 (No. 2021YFG0258), National Natural Science Foundation of China (No. 42001100).

#### 525 **References**

- 526 Adams, B., Fraser, H., Howard, C., Hanafy, M. (1986). Meteorological data analysis for drainage  
527 system design. *J. Environ. Eng.* 112
- 528 Baum, R.L., Savage, W.Z., and Godt, J.W. (2002). TRIGRS-a FORTRAN program for transient  
529 rainfall infiltration and grid-based regional slope stability analysis, Virginia, US Geological  
530 Survey Open file report, 02-424.



- 531 Baum, R.L., Savage, W.Z., and Godt, J.W. (2008). TRIGRS-a FORTRAN program for transient  
532 rainfall infiltration and grid-based regional slope stability analysis, Virginia, US Geological  
533 Survey Open file report, 2008-1159.
- 534 Bel, C., Liébault, F., Navratil O., Eckert N., Bellot H., Fontaine, F., Laigle, D. (2017). Rainfall  
535 control of debris-flow triggering in the Réal Torrent, Southern French Prealps, 291, 17-32.
- 536 Berti, M., Bernard, M., Gregoretto, C., Simoni, A. (2020). Physical interpretation of rainfall  
537 thresholds for runoff-generated debris flows. *Journal of Geophysical Research-Earth Surface*,  
538 125, e2019JF005513.
- 539 Berti, M., Simoni, A. (2005). Experimental evidences and numerical modelling of debris flow  
540 initiated by channel runoff. *Landslides* 3, 171–182
- 541 Caine, N. (1980). The rainfall intensity-duration control of shallow landslides and debris flows.  
542 *Geogr. Ann. Ser. A Phys. Geogr.*, 62, 23–27.
- 543 Cannon, S., Gartner, J., Wilson, R., Bowers, J., Laber, J. (2008). Storm rainfall conditions for  
544 floods and debris flows from recently burned areas in southwestern Colorado and southern  
545 California. *Geomorphology*, 96, 250-269.
- 546 Castillo, V.M., Gómez-Plaza, A., Martínez-Mena, M. (2003). The role of antecedent soil water  
547 content in the runoff response of semiarid catchments: a simulation approach. *J. Hydrol.*, 284  
548 (1–4), 114–130.
- 549 Chen, C.Y., Chen, T.C., Yu, F.C., Yu, W.H., Tseng, C.C. (2005). Rainfall duration and debris-flow  
550 initiated studies for real-time monitoring. *Environ Geol.*, 47, 715–724.
- 551 Chen, C.W., Oguchi, T., Chen, H., Lin, G.W., (2018). Estimation of the antecedent rainfall period  
552 for mass movements in Taiwan. *Environ. Ear. Sci.*, 77, 184.



- 553 Chmiel, M., Walter, F., Wenner, M., Zhang, Z., Mcardell, B.W., Hibert, C. (2020). Machine  
554 learning improves debris flow warning. *Geophysical Research Letter*, 48, e2020GL090874.
- 555 Church, M., Jakob, M. (2020). What is a debris flood? *Water Resour. Res.*, 56, e2020WR027144.
- 556 Coe, J.A., Kinner, D.A., Godt, J.W. (2008). Initiation conditions for debris flows generated by  
557 runoff at Chalk Cliffs, central Colorado. *Geomorphology*, 3, 270–297.
- 558 Crosta, G.B., Frattini, P. (2003). Distributed modeling of shallow landslides triggered by intense  
559 rainfall. *Nat. Hazards Earth Syst. Sci.*, 3, 81–93.
- 560 Cui, P., Yang, K., Chen, J. (2003). Relationship between occurrence of debris flow and antecedent  
561 precipitation: taking the Jiangjia Gully as an example, China. *J. Soil Water Conserv.*, 1, 11-15  
562 (in Chinese).
- 563 Dahal, R.K., Hasegawa, S. (2008). Representative rainfall thresholds for landslides in the Nepal  
564 Himalaya. *Geomorphology*, 100, 429-443.
- 565 Gabet, E.J., Mudd, S.M. (2006). The mobilization of debris flows from shallow landslides.  
566 *Geomorphology*, 1, 207–218.
- 567 Giannecchini, R., Galanti, Y., D'Amato, A. G. (2012). Critical rainfall thresholds for triggering  
568 shallow landslides in the Serchio River valley (Tuscany, Italy). *Nat. Hazards Earth Syst. Sci.*, 12,  
569 829-842.
- 570 Glade, T., Crozier, M.J., Smith, P. (2000). Applying probability determination to refine landslide-  
571 triggering rainfall thresholds using an empirical “Antecedent Daily Rainfall Model”. *Pure Appl.*  
572 *Geophys.*, 157, 1059–1079.
- 573 Guo, X.J., Cui, P., Li, Y. (2013). Debris flow warning threshold based on antecedent rainfall: a  
574 case study in Jiangjia Ravine, Yunnan, China. *J. Mount. Sci.*, 10, 305-314.



- 575 Guzzetti, F., Peruccacci, S., Rossi, M., Strak, C.P. (2008). The rainfall intensity–duration control  
576 of shallow landslides and debris flows: an update. *Landslides*, 5, 3-17.
- 577 Hasnawir, Kubota, T. (2008). Analysis of critical value of rainfall to induce landslides and debris-  
578 flow in Mt. Bawakaraeng Caldera, South Sulawesi, Indonesia. *J. Fac. Agric. Kyushu Univ.*, 53,  
579 523-527.
- 580 Hirschberg, J., Badoux, A., McArdell, B.W., Leonarduzzi, E., Molnar, P. (2021). Evaluating  
581 methods for debris-flow prediction based on rainfall in an Alpine catchment. *Nat. Hazards Earth*  
582 *Syst. Sci.* 21, 2773-2789.
- 583 Iverson, R. M., Reid, M. E., LaHusen, R. G. (1997). Debris flow mobilization from landslides.  
584 *Annu. Rev. Earth Planet*, 25, 85-138.
- 585 Jacobs L., Kervyn, M., Reichenbach, P., Rossi, M., Marchesini, I., Alvioli, M., Dewitte, O., 2020.  
586 Regional susceptibility assessments with heterogeneous landslide information: Slope unit- Vs.  
587 pixel-based approach. *Geomorphology*, 356: 107084.
- 588 Jiang, Z.Y., Fan, X.M., Subramanian, S.S., Yang, F., Tang, R., Xu, Q., Huang, R.Q. (2021).  
589 Probabilistic rainfall thresholds for debris flows occurred after the Wenchuan earthquake using  
590 a Bayesian technique. *Eng. Geo.*, 280, 105965.
- 591 Jones, R., Thomas, R.E., Peakall, J., Manville, V. (2017). Rainfall-runoff properties of tephra:  
592 Simulated effects of grain-size and antecedent rainfall. *Geomorphology*, 282, 39-51.
- 593 Khan, Y.A., Latch, H., Baten, M.A., Kamil, A.A. (2012). Critical antecedent rainfall conditions for  
594 shallow landslides in Chittagong City of Bangladesh. *Environ. Earth Sci.*, 67, 97-106.
- 595 Kim, S.W., Chun, K.W., Kim, M., Catani, F., Choi, B., Seo, J. (2021). Effect of antecedent rainfall  
596 conditions and their variations on shallow landslide-triggering rainfall thresholds in South



- 597 Korea. *Landslides*, 18, 569-582.
- 598 Kim, S.K., Hong, W.P., Kim, Y.M. (1991). Prediction of rainfall-triggered landslides in Korea. In:  
599 Bell DH (ed) *Landslides, Proceedings of the 6th International Symposium on Landslides*, vol 2.  
600 Balkema, Rotterdam, pp 989-994.
- 601 Le Bissonnais, Y., Renaux, B., Delouche, H. (1995). Interactions between soil properties and  
602 moisture content in crust formation, runoff and interrill erosion from tilled loess soils. *Catena*,  
603 25(1), 33-46.
- 604 Lehmann, P., Or, D. (2012) Hydromechanical triggering of landslides: From progressive local  
605 failures to mass release. *Water Resour. Res.*, 48, W03535.
- 606 Liu, D.L., Zhang, S.J., Yang, H.J., Zhao, L.Q., Jiang, Y.H., Tang, D., Leng, X.P. (2016).  
607 Application and analysis of debris-flow early warning system in Wenchuan earthquake-affected  
608 area. *Nat. Hazards Earth Syst. Sci.*, 16, 483-496.
- 609 Long, K., Zhang, S.J., Wei, F.Q., Hu, K.H., Zhang, Q., Luo, Y. (2020). A hydrology-process based  
610 method for correlating debris flow density to rainfall parameters and its application on debris  
611 flow prediction. *Journal of Hydrology*, 589, 125124.
- 612 Luk, S.H. (1985). Effect of antecedent soil moisture content on rainwash erosion. *Catena*, 12, (2-  
613 3), 129-139.
- 614 Marno, P., Peres, D.J., Cancelliere, A., Greco, R., Bogaard, T.A. (2020). Soil moisture information  
615 can improve shallow landslide forecasting using the hydrometeorological threshold approach.  
616 *Landslides*, 17, 2041-2054.
- 617 Marra, F., Destro, E., Nikolopoulos, E.I., Zoccatelli, D., Creutin, J.D., Guzzetti, F., Borga, M.  
618 (2017). Impact of rainfall spatial aggregation on the identification of debris flow occurrence



- 619 thresholds. *Hydrol. Earth Syst. Sci.*, 21, 4525-4532.
- 620 Minder, J.R., Roe, G.H., Montgomery, D.R. (2009). Spatial patterns of rainfall and shallow  
621 landslide susceptibility. *Water Resour. Res.*, 45, W04419.
- 622 Oorthuis, R., Hurlimann, M., Abanco, C., Moya, J., Carleo, L. (2021). Monitoring of rainfall and  
623 soil moisture at the Rebaixader catchment (Central Pyrenees). *Environmental & Engineering  
624 Geoscience*, 27(2), 221-229.
- 625 Papa, M.N., Medina, V., Ciervo, F., Bateman, A. (2013). Derivation of critical rainfall thresholds  
626 for shallow landslides as a tool for debris flow early warning systems. *Hydrol. Earth Syst. Sci.*  
627 17, 4095-4107.
- 628 Peres, D.J., Cancelliere, A. (2014). Derivation and evaluation of landslide-triggering thresholds by  
629 a Monte Carlo approach. *Hydrol. Earth Syst. Sci.*, 18, 4913-4931.
- 630 Raia, S., Alvioli, M., Rossi, M., Baum, R.L., Godt, J.W., Guzzetti, F., 2014. Improving predictive  
631 power of physically based rainfall-induced shallow landslide models: a probabilistic approach,  
632 *Geosci. Model Dev.*, 7, 495-514.
- 633 Richards, L.A., 1931. Capillary condition of liquids in porous mediums. *Physics* 1, 318-333.
- 634 Ruetze, J.V., Lehmann, P., Or, D. (2014) Effects of rainfall spatial variability and intermittency on  
635 shallow landslide triggering patterns at a catchment scale. *Water Resour. Res.*, 50, 7780-7799.
- 636 Segoni, S., Piciullo, L., Gariano, S.L. (2018). A review of the recent literature on rainfall  
637 thresholds for landslide occurrence. *Landslides*, 15, 1483-1501.
- 638 Theule, J.I., Liébault, F., Laigle, D., Loye, A., Jaboyedoff, M. (2015). Channel scour and fill by  
639 debris flows and bedload transport. *Geomorphology*, 243, 92-105.
- 640 Tisdall, A. (1951). Antecedent soil moisture and its relation to infiltration. *Aust. J. Agric. Res.*, 2



- 641 (3), 342–348.
- 642 Yang, H.J., Wei, F.Q., Ma, Z.F., Gao, H.Y., Su, P.C., Zhang, S.J. (2020). Rainfall threshold for  
643 landslide activity in Dazhou, southwest China. *Landslides*, 17, 61-77.
- 644 Zhang, S.J., Jiang, Y.H., Yang, H.J., Liu, D.L. (2015). An hydrology-process based method for  
645 antecedent effect rainfall determination in debris flow forecasting. *Adv. Water Sci.*, 26, 35-43.  
646 (In Chinese)
- 647 Zhang, S.J., Ma, Z.G., Li, Y.J., Hu, K.H., Zhang, Q., Li, L. (2021). A grid-based physical model to  
648 analyze the stability of slope unit. *Geomorphology*, 391, 107887.
- 649 Zhang, S.J., Wei, F.Q., Liu, D.L., Yang, H.J., Jiang, Y.H. (2014b). A regional-scale method of  
650 forecasting debris flow events based on water-soil coupling mechanism. *J. Mount. Sci.*, 6, 1531-  
651 1542.
- 652 Zhang, S.J., Xu, C.X., Wei, F.Q., Hu, K.H., Xu, H., Zhao, L.Q., Zhang, G.P. (2020). A physics-  
653 based model to derive rainfall intensity-duration threshold for debris flow. *Geomorphology*, 351,  
654 106930.
- 655 Zhang, S.J., Yang, H.J., Wei, F.Q., Jiang, Y.H., Liu, D.L. (2014a). A model of debris flow forecast  
656 based on the water-soil coupling mechanism. *J. Earth Sci.*, 4, 757-763.
- 657 Zhang, S.J., Zhao, L.Q., Delgado Tellez, R., Bao, H.J. (2018). A physics-based probabilistic  
658 forecasting model for rainfall-induced shallow landslides at regional scale. *Nat. Hazards Earth  
659 Syst. Sci.*, 18, 969-982.
- 660 Zhao, B.R., Dai, Q., Han, D.W., Dai, H.C., Mao, J.Q., Mao, J.Q., Zhuo, L. (2019). Probabilistic  
661 thresholds for landslides warning by integrating soil moisture conditions with rainfall thresholds.  
662 *Journal of Hydrology*, 574, 276-287.